Complex domain nonlocal block-matching denoising based on high-order singular value decomposition (HOSVD)

Vladimir Katkovnik, Mykola Ponomarenko and Karen Egiazarian
Laboratory of Signal Processing, Tampere University of Technology, P.O. Box 553
FI-33101 Tampere, Finland
e-mails: vladimir.katkovnik@tut.fi, mykola.ponomarenko@tut.fi, karen.egiazarian@tut.fi

***Abstract*—Block matching 3D collaborative filtering (BM3D) is one of the most popular denoising technique based on data sparsity concept applied to specially structured data. In this paper we develop this technique for complex domain, i.e. for application to complex-valued data. Sparsity as an approximation technique can be addressed directly to complex-valued variables or to real-valued pairs phase/amplitude and real/imaginary parts of complex-valued variables. As a result we arrive to various ways of development and obtain a set of quite different algorithms. The algorithms proposed in this paper are composed from two components: nonlocal patch-wise grouping and high-order singular value decomposition (HOSVD) for grouped data processing. The latter gives data adaptive complex-valued bases for complex-valued data or real-valued bases for joint processing of the pairs phase/amplitude, real/imaginary parts of complex-valued variables. Comparative study of the developed algorithms is produced in order to select the most efficient ones.**

I. Introduction

This paper is focussed on a special wide class of image/data processing problems dealing with complex-valued variables. In particular, in optics a monochromatic wavefront is modelled as complex amplitude of the form $u_o(x) = a_o(x)\exp(i\varphi_o(x))$, where amplitude $a_o(x)$ and phase $\varphi_o(x)$ are unknown variables of interest. The areas of applications are from astronomy and engineering to medicine and biology with the main focus on phase reconstruction or *phase imaging*. Phase imaging is one of the key instruments in optics allowing to make visible invisible features of specimens and produce precise measurements with resolution on the level of wavelengths. It is possible due to a phase sensitivity of coherent wavefront to shape and internal structure of specimens. The wavefront phase cannot be measured directly because all measurement instruments are sensitive with respect to the intensity but not to phase. For instance, in interferometry and holography a measured intensity has a form [1]:

$$I(x) = |u_o(x) + u_r(x)|^2, \tag{1}$$

where $u_o(x)$ and $u_r(x)$ stand for object and reference wavefronts, respectively, and $I(x)$ is a measured intensity (power).

For monochromatic coherent imaging both object and reference wavefronts are complex-valued:

$$\begin{aligned} u_o(x) &= a_o(x)\exp(i\varphi_o(x)), \\ u_r(x) &= a_r(x)\exp(i\varphi_r(x)). \end{aligned} \tag{2}$$

Then, the phase imaging means a reconstruction of the phase $\varphi_o(x)$ from usually noisy measurements of $I(x)$. In Fig.1 we show phase and amplitude images of a fly's wing as a specimen obtained by the phase-shifting holography. While the laser beam propagates through the wing its phase and amplitude are changing due to variations of refractive index (for phase) and transparency (for amplitude). One may note that while the phase and amplitude images are far from being identical they are correlated and similar patterns can be seen in these images.

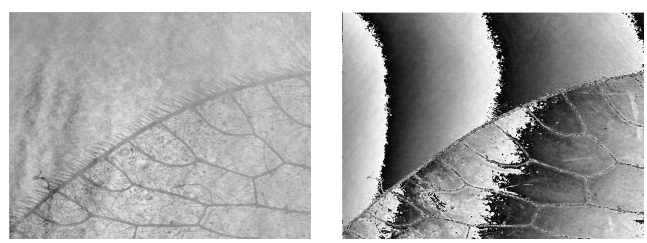

a b

Fig. 1. Fly's wing amplitude (a) and phase (b) images.

In computational imaging sparse and redundant representations have been successfully developed in the last years as a general concept. It is based on the assumption that there exists a small number of items such that image can be represented exactly or approximately with a good accuracy. Here we wish refer to the recent overview [2] of the complex domain sparsity concentrated on applications in optics.

Group (or structured) sparsity. In this technique the *sparsity is introduced artificially by special grouping of observations.* The similarity of the grouped patches enables a high-level sparsity of the grouped data and high efficiency of small-size approximations (e.g. [3], [4]. This kind of techniques became extremely popular after the work on Block Matching 3D (BM3D) filtering [5]. Recently the group sparsity concept

was generalized for the complex domain. In this development the algorithm works directly with complex-valued variables without separation phase and amplitude. The main problem of this development is a design of complex-valued bases enabling the sparsity in the complex domain. It was done in two different ways: the SpInPhase algorithm is based on complex domain dictionary learning with internal and external dictionaries [6] and the BM3D based algorithm uses High-Order Singular Value Decomposition (HOSVD) [7], [8].

The complex-valued u_o can be considered as a function of two pairs of real-valued variables: amplitude and phase, a_o, φ_o, and real and imaginary parts of u_o, $\mathrm{Re}(u_o) = a_o \cos\varphi_o$, $\mathrm{Im}(u_o) = a_o \sin\varphi_o$.

Respectively, the sparsity for the complex-valued u_o can be imposed in the following three different types:

(I) Complex domain sparsity treating u_o as a complex-valued variable;

(II) Sparsity imposed on two real-valued variables: amplitude and phase, a_o, φ_o;

(III) Sparsity imposed on two real-valued variables: real and imaginary parts of u_o, $\mathrm{Re}(u_o) = a_o \cos\varphi_o$, $\mathrm{Im}(u_o) = a_o \sin\varphi_o$.

In the last two cases the sparsity is assumed for $2D$ vectorial real-valued variables. For comparison of different types of sparsity we compare their efficiency for complex domain denoising, i.e. retrieval of the complex-valued $u_o(x)$ from noisy data given with complex-valued noise. Denoising of phase and amplitude is appeared as an avoidable routine in many algorithms and often can be formalized to considered complex domain setting.

Extensive researches in image processing show that a good denoiser can be efficiently incorporated in many procedures as *algorithm from the shelf* for various problems. Even more, a denoiser as a component of the algorithm appears as a solution in many variational setups (e.g. [9], [10]).

Thus, the denoising algorithms developed and studied in this paper are of general interest for different applications. The following model is used for the observed data $z : X \to \mathbb{C}$, where $X \subset Z^2$ is $2D$ grid of size $\sqrt{n} \times \sqrt{n}$:

$$z(x) = u_o(x) + \varepsilon(x), \tag{3}$$

where $x \in X$, $u_o(x) \in \mathbb{C}^{\sqrt{n}\times\sqrt{n}}$ is a clean complex-valued object, and $\varepsilon(x) = \varepsilon_I(x) + j\varepsilon_Q(x) \in \mathbb{C}^{\sqrt{n}\times\sqrt{n}}$, is complex-valued zero-mean Gaussian circular white noise of variance σ^2 (i.e., ε_I and ε_Q are zero-mean independent Gaussian random variables with variance $\sigma^2/2$).

The contribution of this paper is two fold. First, a development of novel complex domain denoising algorithms using the three types of the sparsity modeling mentioned above. While the algorithm based on the sparsity Type I has a predecessor proposed in [7], [8] and differs from it by the modified thresholding rules, other algorithms are completely novel. The complex domain Wiener filters are developed as post-processors for these algorithms. Second, extended simulation experiments targeted on the accuracy analysis and the comparison of the algorithms. It is shown that overall the algorithms based on the sparsity Types I and III are enabling the best accuracy.

II. Algorithms

The proposed algorithms copy the structure of the standard BM3D filter as it is introduced in [5]. The difference concerns the following important aspects: the grouping is produced for complex-valued variables instead of the real-valued ones in [5], the transforms used for the data analysis are not fixed as it is in [5] but data adaptive and generated using High-Order Singular Value Decomposition (HOSVD), the input variables of HOSVD are different for different algorithm: complex-valued variables, imaginary and real parts or phase and amplitude of complex-valued variables. Similar to the standard BM3D the proposed algorithms are composed from two stages: thresholding following by Wiener filtering. This new technique can be understood as a generalization for the complex domain of the BM3D-SAPCA algorithm [11], where SVD is used for design of 2D orthonormal bases for patches, and also of HOSVD-BM3D proposed in [12], where HOSVD is exploited as a generator of 3D/4D real domain orthonormal transforms. The flow chart is the same for all proposed algorithms. It is shown in Fig.2.

A. CD-BM3D: COMPLEX DOMAIN SPARSITY (Type I)

1) Thresholding filtering: We start from the algorithm based on complex-domain sparsification of u_o. The abbreviation CD-BM3D is introduced for this algorithm. Here CD (*complex domain*) emphasizes the succession of this algorithm with respect to the standard BM3D.

According to the conventional procedure in patch-based image restoration, the noisy $\sqrt{n} \times \sqrt{n}$ image $\mathbf{z} \equiv \{z(x), x \in X\}$ is partitioned into small overlapping rectangular/square patches $N_1 \times N_2$ defined for each pixel of the image. The algorithm is composed from five basic steps: grouping, collaborative filtering via HOSVD transform (e.g. [13]), hard-thresholding of HOSVD spectrum, inverse HOSVD transform, and aggregation of the overlapping patch estimates. Details of these five steps can be seen in [7], [8]. The flow chart of this algorithm can be seen in the left part of Fig.2.

2) Wiener filtering : The Wiener filter has two input variables: the noisy observation z and the reference variable u^{ref} carrying some information on u_o. Conventionally in many algorithms for instance in BM3D [5] u^{ref} is the output of the thresholding algroithm. The following five steps of the algorithm are similar to the steps of the thresholding algorithm but with a number of modifications.

1. **Grouping.** The grouping is produced for the reference variable u^{ref} giving the groups denoted as $G_r^{u^{ref}}$. In parallel we form the groups from the input variable z. These groups for z are formed exactly accordingly to $G_r^{u^{ref}}$, i.e. the group G_r^z includes the same patches as $G_r^{u^{ref}}$ but taken from z.The matched patches are stacked to form two 3D arrays of size $N_1 \times N_2 \times J_r$ denoted by $\mathbf{Z}_{u^{ref}}^r$ and $\mathbf{Z}_z^r$, respectively.

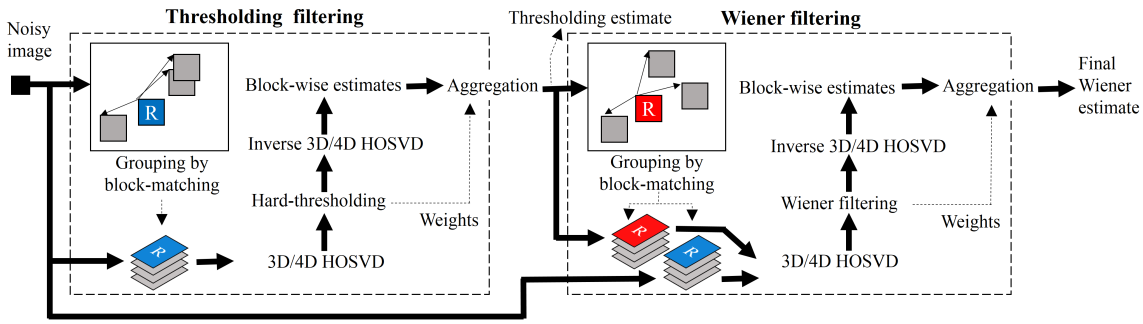

Fig. 2. The flow chart of the proposed complex domain algorithms

2. **3D HOSVD.** The arrays $\mathbf{Z}^r_{u^{ref}}$ and $\mathbf{Z}^r_z$ are used differently. The HOSVD analysis is produced for the reference arrays

$$\mathbf{Z}^r_{u^{ref}} = \mathbf{S}^{u^{ref}}_r \times_1 \mathbf{T}^{ref}_{1,r} \times_2 \mathbf{T}^{ref}_{2,r} \times_3 \mathbf{T}^{ref}_{3,r}, \quad (4)$$

giving the core tensor $\mathbf{S}^{u^{ref}}_r$ (*reference spectrum*) and the transforms $\mathbf{T}^{ref}_{1,r}$, $\mathbf{T}^{ref}_{2,r}$ and $\mathbf{T}^{ref}_{3,r}$.

Further these transform are applied for the analysis of $\mathbf{Z}^r_z$ with the corresponding core spectrum $\mathbf{S}^z_r$ calculated as

$$\mathbf{S}^z_r = \mathbf{Z}^r_z \times_1 (\mathbf{T}^{ref}_{1,r})^T \times_2 (\mathbf{T}^{ref}_{2,r})^T \times_3 (\mathbf{T}^{ref}_{3,r})^T. \quad (5)$$

3. Empirical **Wiener filtering** replaces the thresholdings and gives the filtered version of the core spectrum $\mathbf{S}^z_r$ in the form

$$\hat{\mathbf{S}}^z_r = \frac{|\mathbf{S}^{u^{ref}}_r|^2 \cdot \mathbf{S}^z_r}{|\mathbf{S}^{u^{ref}}_r|^2 + \beta}, \quad (6)$$

where all operations with the tensors are element-wise and $\beta > 0$ is the regularization parameter.

4. **Inverse 3D HOSVD.** The filtered group according to (4) in the image domain is calculated as

$$\hat{\mathbf{U}}^r_z = \hat{\mathbf{S}}^z_r \times_1 \mathbf{T}^{ref}_{1,r} \times_2 \mathbf{T}^{ref}_{2,r} \times_3 \mathbf{T}^{ref}_{3,r}. \quad (7)$$

5. **Aggregation** is produced with the weights g_r calculated as $g_r = 1/||\hat{\mathbf{S}}^z_r||^2_2$.

Here and in what follows the norm $||\cdot||^2_2$ is calculated as the sum of the squared absolute values of all items of the array-argument. The flow chart of this algroithm can be seen in the right part of Fig.2.

B. REAL DOMAIN SPARSITY (Type II and Type III)

In this group of the algorithms the HOSVD based spectrum analysis and transform design are applied to real-valued variables. As it is discussed in Introduction the complex variable sparsity can be thought as the sparsity of the corresponding real-valued variables: phase/amplitude and real/imaginary parts (sparsity Types II and III).

Accordingly, we developed two types of the algorithms. The essential difference with the algorithms presented above concerns HOSVD which is applied to 4D groups instead of 3D groups. This higher dimension allows to design the spectra and transforms which take into consideration correlation between phase and amplitude and real and imaginary parts of the input data. All other steps of the algorithms are exactly as they are in Sections II-A1 and II-A2 for thresholding and Wiener filtering. For the novel algorithms obtained in this way we will use a specific notations: *ImRe-BM3D* and *PhAm-BM3D*, where *ImRe* and *PhAm* indicate what variables are used for transforms and spectrum analysis.

Overall we obtain four different algorithms to be compared in this paper: CD-BM3D with two thresholding schemes (thresholding of the absolute values or real/imaginary parts of spectra) and ImRe-BM3D and PhAm-BM3D. For all these algorithms the corresponding Wiener filters are developed.

III. RESULTS

The developed algorithms are tested by analyzing the accuracy of the phase reconstruction for various phase and amplitude test images. For the interferometric phase the accuracy is measured by the peak signal-to-noise ratio ($PSNR$):

$$PSNR_\varphi = 10 \log_{10} \frac{n(2\pi)^2}{||\mathcal{W}(\hat{\varphi}_o - \varphi_o)||^2_2} [dB], \quad (8)$$

where $\hat{\varphi}_o$ and φ_o are the phase reconstruction and the true phase, respectively; n is the image size; the phase wrapping operator $\mathcal{W}$ is used in order to eliminate the phase shifts in errors multiple to 2π. The factor $(2\pi)^2$ in the nominator of (8) stays for the squared maximum value of the interferometric phase. Being concentrated on the phase reconstruction in our experiments we control the noise level in the observed phase for any kind of amplitude variable $a_o(x)$. The experiments are produced for varying standrad deviation of this noise $\sigma_{\varphi_z} = \{0.05, 0.1, 0.2, 0.5, 0.9\}$. The largest value of σ_{φ_z} corresponds to the very noisy case.

The all results shown in what follows are done for the thresholding algorithms complemented by the Wiener filtering.

For comparison we show also results obtained by the standard BM3D applied independently to real and imaginary parts of z . The abbreviation BM3D for is used for this application of the standard BM3D filter to complex-valued data.

It is of special interest to compare this straightforward application of BM3D to complex-valued data with ImRe-BM3D, where the data adaptive basis is generated by $4D$

$HOSVD$ and correlation between the real and imaginary parts of observations are taken into considerations. It is shown that the proposed algorithms and in particular ImRe-BM3D significantly overperform BM3D.

A. Phase test-images

The test phase images $\varphi_o(x)$ of the size 256×256 are shown in Fig.3. The images lena (a) and cameraman (b) are interferometric phases normalized to the interval $[0, \pi/2]$. The absolute phase corresponding to the images (c) and (d) is the truncated Gaussian distribution with the maximum value equal to 44 radians and zeroed one of the quadrants, what makes this absolute phase discontinuous and more difficult for reconstruction. In image (c) we show the wrapped version of this phase and the absolute phase shown as a 3D surface in image (d).

The "*mountains*" images (e)-(f) are shown as wrapped and 3D absolute phase which is smooth with multiple picks. The range of this phase variations is from -5 to 3.3 radians.

The absolute phase for images (g)-(h) is the sum of the lena phase from image (a) and the quadratic phase with the maximum value 26 radians. In image (g) the lena features are destructed by the fringes of the quadratic phase. In the absolute phase image (h) the lena is nearly invisible due to the larger magnitude of the quadratic phase.

Note that our algorithms deals with wrapped phase variables as they shown in the images (c, e, g) and the absolute phase reconstruction can be obtained by unwrapping the estimate of the corresponding wrapped phase. Closed fringes typical for the wrapped phase are well seen in the images (c, e, g) make the problem of the phase restoration very hard. In order to make a difference between the test images (a,b) and (c)-(f) we will refer the former as an interferometric phase and the latter as a wrapped phase.

B. Amplitude test images

As it is illustrated in Fig.1 typically, e.g. in holography, phase and amplitude images can be quite correlated. For amplitude test images 256×256 we selected invariant and varying functions of different link with the test phase images imitating a dependence between the phase and amplitude appeared in real data, in particular, shown in Fig.1.

C. Complex-valued test images

Combining the introduced phase and amplitude test images we generate a large set of different complex-valued $u_o(x)$. As a result of our preliminary study we selected 20 representative complex-valued models. The first 12 models are used with wrapped phases and the others (13–20) - with interferometric phases. The algorithms are tested for all these 20 complex-valued images and for various σ_{φ_z}.

As an example of our tests we show diagrams in Fig.4 allowing to compare the algorithms for quite noisy data with $\sigma_{\varphi_z} = 0.2$. For the wrapped phase test images $1 \div 12$ the best results are shown mainly by CD-BM3D, while for other tests with the interferometric phase ImRe-BM3D continues to show better accuracy than CD-BM3D.

The average gap between ImRe-BM3D and BM3D increases from 0.6 dB to 1.9 dB as compared with the case $\sigma_{\varphi_z} = 0.05$. To illustrate how significant is this 1.9 dB benefit we show the noisy test image 19 and the results for phase reconstruction obtained by ImRe-BM3D, CD-BM3D and BM3D (see 5).

D. Conclusions

For implementation and algorithm design we use the nonlocal block-matching with structural sparsity developed for 3D/4D tensors obtained by grouping similar patches of complex-valued data. This approach results in the following novel algorithms: CD-BM3D, ImRe-BM3D and PhAm-BM3D, where CD-BM3D uses 3D HOSVD dealing with complex-valued variables directly, while ImRe-BM3D and PhAm-BM3D use 4D HOSVD, respectively, dealing with the pairs phase/ amplitude and real/imaginary parts of complex valued HOSVD spectra. The algorithms are developed in two versions: hard-thresholding and Wiener filtering.

Overall conclusions on comparison are as follows. The Wiener filtering gives improvement in $PSNR_\varphi$ about $0.2 \div 0.3$ dB with respect to the hard-thresholding algorithms. The best accuracy is achieved by two competitive algorithms: CD-BM3D and ImRe-BM3D.

Comparison versus the standard real domain BM3D algorithm applied separately to real and imaginary parts of the complex-valued data is definitely in favor of CD-BM3D and ImRe-BM3D with an PSNR_φ improvement of about $1 \div 2$ dB.

IV. Acknowledgment

This work is supported by Academy of Finland, project no. 287150, 2015-2019.

References

[1] T. Kreis, *Handbook of holographic interferometry: optical and digital methods*. John Wiley & Sons, 2006.

[2] Y. Shechtman, Y. C. Eldar, O. Cohen, H. N. Chapman, J. Miao, and M. Segev, "Phase retrieval with application to optical imaging: a contemporary overview," *IEEE Signal Processing Magazine*, vol. 32, no. 3, pp. 87–109, 2015.

[3] J. Mairal, F. Bach, J. Ponce *et al.*, "Sparse modeling for image and vision processing," *Foundations and Trends® in Computer Graphics and Vision*, vol. 8, no. 2-3, pp. 85–283, 2014.

[4] J. Zhang, D. Zhao, and W. Gao, "Group-based sparse representation for image restoration," *IEEE Transactions on Image Processing*, vol. 23, no. 8, pp. 3336–3351, 2014.

[5] K. Dabov, A. Foi, V. Katkovnik, and K. Egiazarian, "Image denoising by sparse 3-d transform-domain collaborative filtering," *IEEE Transactions on image processing*, vol. 16, no. 8, pp. 2080–2095, 2007.

[6] H. Hongxing, J. M. Bioucas-Dias, and V. Katkovnik, "Interferometric phase image estimation via sparse coding in the complex domain," *IEEE Transactions on Geoscience and Remote Sensing*, vol. 53, no. 5, pp. 2587–2602, 2015.

[7] V. Katkovnik, K. Egiazarian, and J. Bioucas-Dias, "Phase imaging via sparse coding in the complex domain based on high-order svd and nonlocal bm3d techniques," in *Image Processing (ICIP), 2014 IEEE International Conference on*. IEEE, 2014, pp. 4587–4591.

[8] V. Katkovnik and K. Egiazarian, "Sparse phase imaging based on complex domain nonlocal bm3d techniques," *Digital Signal Processing*, vol. 63, pp. 72–85, 2017.

[9] C. A. Metzler, A. Maleki, and R. G. Baraniuk, "From denoising to compressed sensing," *IEEE Transactions on Information Theory*, vol. 62, no. 9, pp. 5117–5144, 2016.

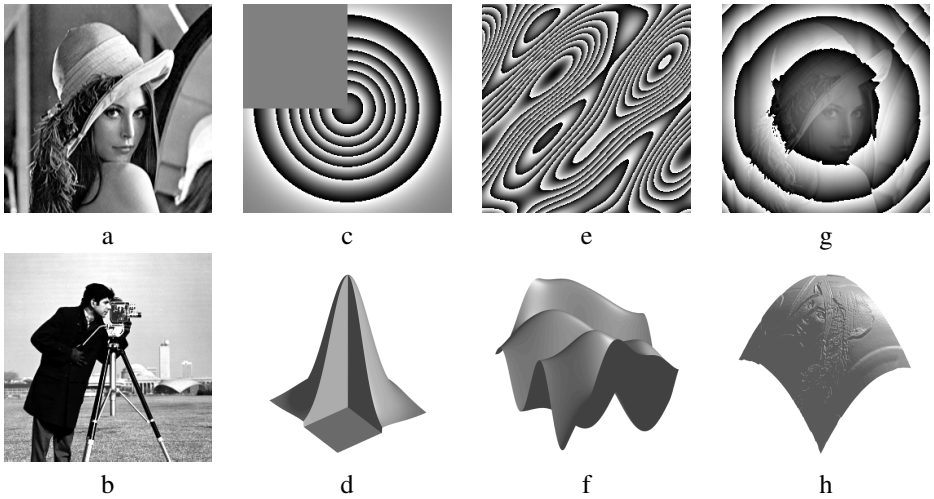

Fig. 3. Test phase images

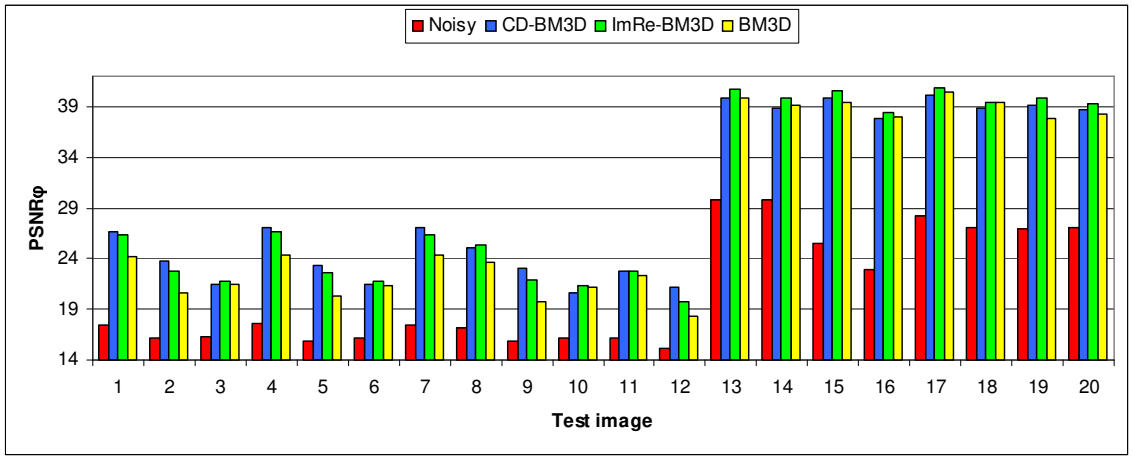

Fig. 4. $PSNR_\varphi$ values for noisy data, CD-BM3D, ImRe-BM3D and BM3D, $\sigma_{\varphi_z} = 0.2$.

Fig. 5. Test image 19: a) noisy phase for σ_{φ_z}=0.2, $PSNR_\varphi$=26.9 dB, b) phase reconstruction by CD-BM3D, $PSNR_\varphi$=39.1 dB, c) phase reconstruction by ImRe-BM3D, $PSNR_\varphi$=39.8 dB, d) phase reconstruction by BM3D, $PSNR_\varphi$=37.8 dB,.

[10] A. Danielyan, V. Katkovnik, and K. Egiazarian, "Bm3d frames and variational image deblurring," *IEEE Transactions on Image Processing*, vol. 21, no. 4, pp. 1715–1728, 2012.

[11] A. Foi, V. Katkovnik, and K. Egiazarian, "Pointwise shape-adaptive dct for high-quality denoising and deblocking of grayscale and color images," *IEEE Transactions on Image Processing*, vol. 16, no. 5, pp. 1395–1411, 2007.

[12] A. Rajwade, A. Rangarajan, and A. Banerjee, "Image denoising using the higher order singular value decomposition," *IEEE Transactions on Pattern Analysis and Machine Intelligence*, vol. 35, no. 4, pp. 849–862, 2013.

[13] L. De Lathauwer, B. De Moor, and J. Vandewalle, "A multilinear singular value decomposition," *SIAM journal on Matrix Analysis and Applications*, vol. 21, no. 4, pp. 1253–1278, 2000.